$Au_{25}(SEt)_{18}$, a Nearly Naked Thiolate-Protected Au_{25} Cluster: Structural Analysis by Single Crystal X-ray Crystallography and Electron Nuclear Double Resonance

Tiziano Dainese,[†] Sabrina Antonello,[†] José A. Gascón,[‡] Fangfang Pan,[⊥] Neranjan V. Perera,[‡] Marco Ruzzi,[†] Alfonso Venzo,[†,§] Alfonso Zoleo,[†] Kari Rissanen,[⊥,*] and Flavio Maran[†,*]

[†]Department of Chemistry, University of Padova, via Marzolo 1, 35131 Padova, Italy, [‡]Department of Chemistry, University of Connecticut, 55 North Eagleville Road, Storrs, Connecticut 06269, United States, [§]IENI-CNR c/o Department of Chemistry, University of Padova, via Marzolo 1, 35131 Padova, Italy, and [⊥]Department of Chemistry, Nanoscience Center, University of Jyväskylä, P.O. Box 35, 40014 JYU, Finland

ABSTRACT X-ray crystallography has been fundamental in discovering fine structural features of ultrasmall gold clusters capped by thiolated ligands. For still unknown structures, however, new tools capable of providing relevant structural information are sought. We prepared a 25-gold atom nanocluster protected by the smallest ligand ever used, ethanethiol. This cluster displays the electrochemistry, mass spectrometry, and UV–vis absorption spectroscopy features of similar Au_{25} clusters protected by 18 thiolated ligands. The anionic and the neutral form of $Au_{25}(SEt)_{18}$ were fully characterized by ^{1}H and ^{13}C NMR spectroscopy, which confirmed the monolayer's properties and the paramagnetism of neutral $Au_{25}(SEt)_{18}^{0}$. X-ray crystallography analysis of the latter provided the first known structure of a gold cluster protected by a simple, linear alkanethiolate. Here, we also report the direct observation by electron nuclear double resonance (ENDOR) of hyperfine interactions between a surface-delocalized unpaired electron and the gold atoms of a nanocluster. The advantages of knowing the exact molecular structure and having used such a small ligand allowed us to compare the experimental values of hyperfine couplings with DFT calculations unaffected by structure's approximations or omissions.

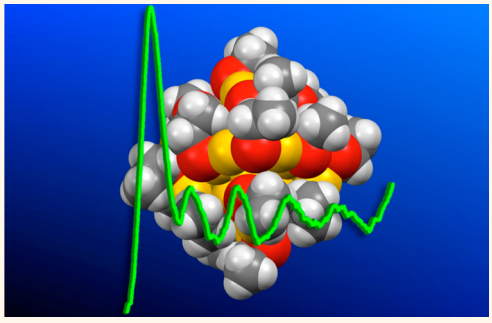

KEYWORDS: gold nanoclusters · Au_{25} · $Au_{25}(SEt)_{18}$ · X-ray crystallography · ENDOR · paramagnetism

Formation of different thiolate-protected gold clusters is a delicate balance of thiol selection, relative concentrations, experimental conditions, and modus operandi.[1−4] As for the analogous self-assembled monolayers (SAMs) of thiols on flat gold surfaces,[5] interaction of the thiolated heads with the surface gold atoms yields interesting structural features.[6−8] For monolayer-protected gold clusters (MPCs), single crystal X-ray crystallography has provided evidence and details of both the inner gold-core structures and the staple-like, half-crown motifs by which the outermost gold atoms interact with sulfur atoms. For homogeneous series of thiolate ligands (SR), the structures so far identified crystallographically are $Au_{102}(SR)_{44}$,[9] $Au_{38}(SR)_{24}$,[10] $Au_{36}(SR)_{24}$,[11] $Au_{28}(SR)_{20}$,[12] $Au_{25}(SR)_{18}$,[13−15] and $Au_{23}(SR)_{16}$.[16] Noteworthy, in none of these structures the ligands were simple linear alkanethiols but rather were aryl and arene-type thiols (phenylethanethiol, 4-*tert*-butylbenzenethiol, 4-mercaptobenzoic acid) or a hindered alkanethiol (cyclohexanethiol). Indeed, due to the intrinsic complexity of MPCs, particularly because of the conformational mobility that ligands may experience, successful preparation of crystals suitable for X-ray diffraction analysis and atomic structure determination is a very challenging task. Devising alternative approaches suitable for obtaining relevant structural information is thus of outmost importance.

Independently of the approach employed, the necessary starting point is identification

* Address correspondence to flavio.maran@unipd.it, kari.t.rissanen@jyu.fi.

Received for review February 10, 2014 and accepted March 15, 2014.

Published online March 15, 2014
10.1021/nn500805n

of the chemical formula. Mass spectrometry techniques proved to be very effective, particularly matrix-assisted laser desorption ionization time-of-flight (MALDI-TOF) mass spectrometry[17] and electrospray ionization (ESI) mass spectrometry.[18,19] Mass spectra were indeed instrumental to establish the correct cluster formula in advance of the actual structural determination for $Au_{25}(SR)_{18}$,[18,19] formerly believed to be $Au_{38}(SR)_{24}$.[20] Very recently, structural characteristics of clusters whose single crystal X-ray diffraction structure is still unknown were inferred by different approaches. Rapid electron diffraction in scanning transmission electron microscopy (STEM) was employed to gain insights into the structure of $Au_{130}(SR)_{50}$,[21] a gold MPC very recently reported,[22,23] and $Au_{144}(SR)_{60}$.[24] In both cases, structural analysis was supported by the good agreement with density functional theory (DFT) calculations.[21,24] Structural information about $Au_{144}(SR)_{60}$ was also obtained by a combination of infrared spectroscopy, ^{13}C NMR spectroscopy, and X-ray diffraction of a single crystal.[25]

$Au_{25}(SR)_{18}$ is the most well-known and characterized MPC displaying a distinct molecule-like behavior.[20] The latter is evident from its characteristic UV−vis absorption spectrum that provides the energy gap between the highest occupied molecular orbital (HOMO) and lowest unoccupied molecular orbital (LUMO).[26] The spectrum depends on the charge state and so does the HOMO−LUMO gap.[27] Sensitive electrochemical methods such as cyclic voltammetry and differential pulse voltammetry show series of peaks marking the stepwise charging of the gold core, and allow estimating the electrochemical HOMO−LUMO gap that upon correction for charging energy furnishes essentially the same gap energy.[26,28] These charge states display quite different stability.[27] One-electron oxidation of the as-prepared cluster, a diamagnetic anionic species, generates a paramagnetic species. The latter displays a distinct electron paramagnetic resonance (EPR) behavior,[27,29] best detected at liquid helium temperatures, and very particular ^{1}H and ^{13}C NMR spectroscopy patterns.[30,31] The above discussion shows that a crucial feature to obtain reliable insights into the properties of molecule-like MPCs is to prepare them in a truly monodisperse form, with atomic precision. Overall, $Au_{25}(SR)_{18}$ is thus the ideal candidate for testing new concepts, techniques, and methodologies to investigate structural properties of molecule-like and possibly larger clusters.

Here, we describe a new strategy to address these issues. We prepared a monodisperse Au_{25} cluster protected by the smallest ligand ever used, ethanethiol. $Au_{25}(SEt)_{18}$ was fully characterized by MALDI-TOF, UV−vis, electrochemistry, and ^{1}H and ^{13}C NMR spectroscopy of both the anion and the neutral forms. Successful preparation of high-purity samples and single crystals allowed us to obtain the first X-ray structure of a gold cluster protected by a very short alkanethiolate. For this purpose, we used the neutral cluster, $Au_{25}(SEt)_{18}^{0}$, and found that the gold and sulfur atoms are structurally arranged as previously described for $Au_{25}(SC_2H_4Ph)_{18}^{0}$ and $Au_{25}(SC_2H_4Ph)_{18}^{-}$,[13−15] but also with some differences around the Au_{13} icosahedral core. We focused on using a very short thiol ligand also because of the possibility of carrying out particularly accurate DFT calculations, that is, with fewer approximations than required for describing more complex ligand systems.

We then used frozen glassy solutions (at 5.5 K) of paramagnetic $Au_{25}(SEt)_{18}^{0}$ to obtain the first electron nuclear double resonance (ENDOR) results for an MPC. ENDOR is a superhyperfine technique able to determine hyperfine coupling constants that are unresolved in the continuous wave EPR (cw-EPR) spectra.[32] Pulse ENDOR is a particularly sensitive method of performing ENDOR.[33] ENDOR is especially suited to elucidate hyperfine interactions between an unpaired electron and surrounding nuclei. Each group of equivalent magnetic nuclei with nuclear spin $I = 1/2$ gives rise to a doublet of lines in the ENDOR spectrum, independently of the number of equivalent nuclei coupled to the electron spin. If the hyperfine coupling A is smaller than twice the nucleus Larmor frequency ν, the doublet is centered at ν and the two lines are separated by A. If $A > 2\nu$, the doublet is centered at $A/2$ and the two lines are separated by 2ν. For a nuclear spin larger than 1/2, the quadrupolar interaction affects the ENDOR spectra by further splitting the ENDOR lines. This is indeed the case of ^{197}Au ($I = 3/2$), which exhibits both quadrupolar and hyperfine interaction.[34] $Au_{25}(SEt)_{18}^{0}$ showed a very nice ENDOR pattern that enabled us to determine the hyperfine interaction between the unpaired electron and the gold atoms. Through knowledge of the exact 3D structure of $Au_{25}(SEt)_{18}^{0}$, we carried out a specific DFT study aimed to determine the relevant isotropic and anisotropic hyperfine coupling constants. A good match of the outcome of DFT calculations and ENDOR results was observed, which allowed assigning each ENDOR signal to specific types of Au atoms forming the cluster. Our results show that ENDOR is a valuable technique that can be successfully employed for obtaining relevant information about the fine structure and the electronic distribution of nanoclusters.

RESULTS AND DISCUSSION

Synthesis and Characterization of $Au_{25}(SEt)_{18}$. The synthesis of $Au_{25}(SEt)_{18}$ was carried out as detailed in the Experimental Section. Briefly, addition of ethanethiol to a red tetrahydrofuran solution of tetrachloroauric acid (molar ratio 4:1) and tetra-*n*-octylammonium bromide (1.2 equiv) eventually yielded a colorless solution of reactive Au(I)-thiolate species. Reduction to Au(0) was carried out by addition of aqueous sodium

borohydride. After 2 days under stirring, the clusters were separated from the reaction mixture and purified. $Au_{25}(SEt)_{18}$, initially obtained as [*n*-Oct_4N^+][$Au_{25}(SEt)_{18}^-$], was eventually oxidized to $Au_{25}(SEt)_{18}^0$ by silica-gel column chromatography under aerobic conditions. The anionic and neutral forms show the UV−vis spectra expected for $Au_{25}(SR)_{18}$ clusters (Figure S1 in Supporting Information).[15,26,30] The chemical composition, purity, and monodispersity of $Au_{25}(SEt)_{18}^0$ were assessed by MALDI-TOF mass spectrometry.[31] In particular, the spectrum of the purified sample shows a peak centered at 6024 that corresponds to the unfragmented cluster. The main fragmentation pattern, which increases as the laser intensity increases, reveals stepwise loss of four AuSEt units (mass = 258.1) to form $Au_{21}(SEt)_{14}$ (mass = 4992) (Figure S2 in Supporting Information).

Electrochemistry. The electrochemical behavior of $Au_{25}(SEt)_{18}$ was studied in a dichloromethane (DCM) solution containing 0.1 M tetra-*n*-butylammonium hexafluorophosphate (TBAH). The electrochemical pattern is quite similar to that of $Au_{25}(SC_2H_4Ph)_{18}$, *i.e.*, two main reversible peaks O1 and R1 associated with the +1/0 and 0/−1 redox couples, and further oxidation or reduction peaks corresponding to formation of higher positive or negative charge states.[26] In cyclic voltammetry (CV), the latter are chemically irreversible. For example, Figure 1A, obtained starting from $Au_{25}(SEt)_{18}^0$, shows that the peak current of the irreversible peak R2 is much larger than that of R1; as a matter of fact, its peak current corresponds to *ca.* 5 electron/molecule at 0.1 V s^{-1}, a value larger than that of *ca.* 3.5 electron/molecule observed for $Au_{25}(SC_2H_4Ph)_{18}$.[28] Peaks R2 and O2 can be made reversible by increasing the CV scan rate and/or lowering the temperature. Figure 1B, obtained starting from $Au_{25}(SEt)_{18}^-$, shows the situation observed for O2 (and O3) at −49 °C, in which O2 is partially reversible. By carrying out CV analysis of the peaks, according to previously described methodologies,[27,28] the lifetimes of the corresponding electrogenerated species (at 25 °C) were estimated to be 0.11 s and 3 ms for O2 and R2, respectively. Comparison with the values of 0.33 s (O2) and 4 ms (R2) measured for $Au_{25}(SC_2H_4Ph)_{18}$ under similar experimental conditions shows that the ethanethiolate ligands make the higher charge states less chemically stable. The lability of the species generated at O2 and R2, conceivably a radical dication and a radical dianion,[27] respectively, is thus incompatible with their use in NMR and, particularly, ENDOR experiments. In the following, we will thus focus on the only stable radical state, $Au_{25}(SEt)_{18}^0$.

NMR Spectroscopy. The ^{1}H NMR spectrum of an acetonitrile-d_3 solution of [*n*-Oct_4N^+][$Au_{25}(SEt)_{18}^-$] shows two sharp CH_3-CH_2 typical patterns (triplet and quartet), together with signals associated with the tetra-*n*-octylammonium countercation (Figure 2A). When taking the area of the ammonium $N-CH_2$ resonance (3.05 ppm) as a standard for integration, the resonances at 1.30 and 2.94 ppm pertain to CH_3 and CH_2 of the 6 ethyl groups of the outer ligands,

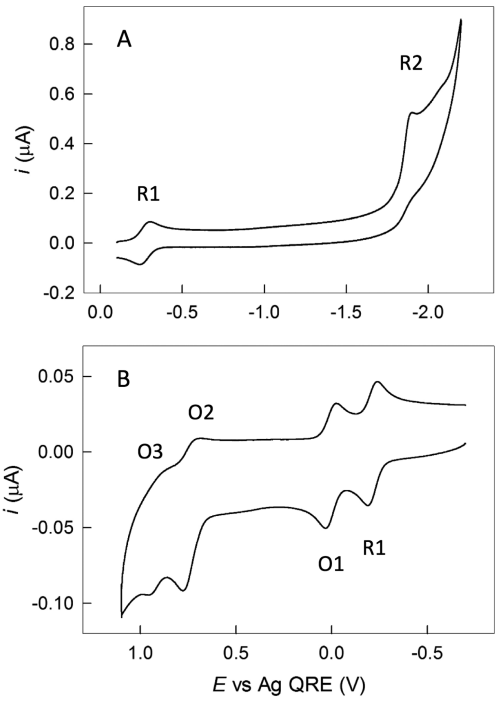

Figure 1. CV pattern for (A) the reduction of 0.32 mM $Au_{25}(SEt)_{18}^0$ at 25 °C and (B) the oxidation of 0.30 mM $Au_{25}(SEt)_{18}^-$ at −49 °C in DCM/0.1 M TBAH, on a glassy carbon electrode at 0.2 V s^{-1}. The peaks are labeled according to electron uptake or release by the neutral cluster.

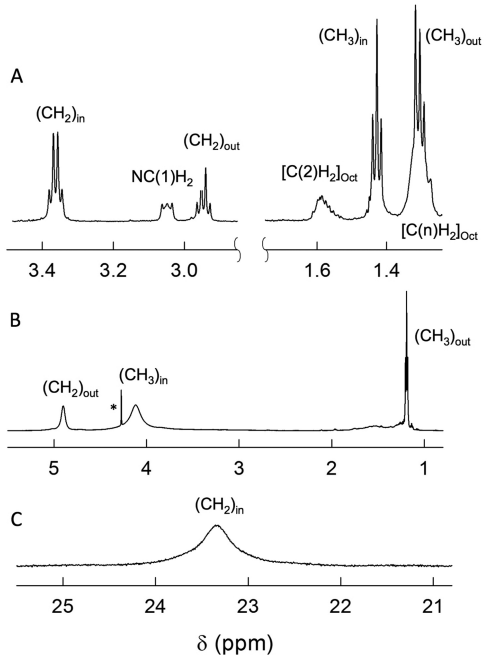

Figure 2. ^{1}H NMR spectra of (A) [*n*-$(Oct)_4N^+$] [$Au_{25}(SEt)_{18}^-$] in acetonitrile-d_3 at 25 °C, and $Au_{25}(SEt)_{18}^0$ in benzene-d_6 (B) at 25 and (C) 65 °C. The spectra show the relevant zones and resonances, including some peaks of *n*-$(Oct)_4N^+$, as indicated. The asterisk (*) marks an impurity (DCM).

whereas the corresponding resonances of the 12 ethyl groups of the inner ligands are found at 1.43 and 3.36 ppm. It is worth noting that a larger shielding is experienced by the groups belonging to the outer ligands, and that the integrals confirm the inner-to-outer ligand 2:1 ratio. The corresponding ^{13}C resonances are observed at 33.21 $(CH_2)_{in}$ and 21.88 ppm $(CH_3)_{in}$, and 29.27 $(CH_2)_{out}$ and 19.88 ppm $(CH_3)_{out}$.

For solubility reasons, the spectra of $Au_{25}(SEt)_{18}^0$ were obtained in benzene-d_6 (Figure 2B). This neutral cluster is expected to be a radical, and as a matter of fact, the resonances of both its outer and inner ligands are broadened due to proximity with the paramagnetic metal center. The COSY-correlated CH_3-CH_2 resonances of the outer ligands are at 1.19 and 4.83 ppm, respectively, whereas those of the corresponding inner groups are 4.12 (CH_3) and 23.4 ppm (CH_2, measured at 65 °C). The highly deshielded $(CH_2)_{in}$ resonance is very broad at 25 °C (*ca.* 3000 Hz) but becomes sharper as the temperature is increased to 65 °C, at which a COSY correlation with the CH_3 signal at 4.12 ppm is detected. Under these conditions, the corresponding integrals are in very good agreement with the expected inner-to-outer ligand 2:1 ratio. The ^{13}C resonances of the outer ligands are detected at 28.0 (CH_3) and 35.5 ppm (CH_2). On the other hand, the very long instrumental time (at least 48 h at 65 °C) required for observing the very broad ^{13}C resonances of the inner ligands induces extensive sample decomposition. The general NMR behavior of $Au_{25}(SEt)_{18}^0$ is thus in keeping with that of other paramagnetic $Au_{25}(SR)_{18}^0$ clusters.[30,31]

The X-ray Structure. The X-ray single-crystal diffraction experiment confirmed the compositional and structural deduction from the mass spectrometry, the electrochemical, and the spectral analyses. The crystals used for X-ray crystallographic study were obtained by diffusing diisopropyl ether vapor into the toluene solution containing $Au_{25}(SEt)_{18}^0$. The compound crystallizes in a centrosymmetric triclinic space group $P\bar{1}$, with the central Au atom at the inversion center, as observed for $Au_{25}(SC_2H_4Ph)_{18}^0$.[15] The central Au atom is surrounded by 12 Au atoms. These 13 atoms form the inner (body-centered) icosahedral core (Figure 3A). The Au–Au bond distances between the central Au atom and the 12 inner layer Au atoms vary very little and are between 2.785 and 2.801 Å. In addition to being bound to the central Au atom, each of the 12 inner shell Au atoms is coordinated to five icosahedron Au atoms and one S atom. Interestingly, whereas six of them are also bound to three stellated Au atoms, the remaining six atoms show interactions only with two stellated Au atoms. In other words, the staples are distorted so that whereas one of the two Au(stellated)–Au(icosahedron) distances is, on average, 3.315 Å, the second one is 3.241 Å (the latter is evidenced as a bond in Figure 3). This kind of dissymmetry is not observed in the

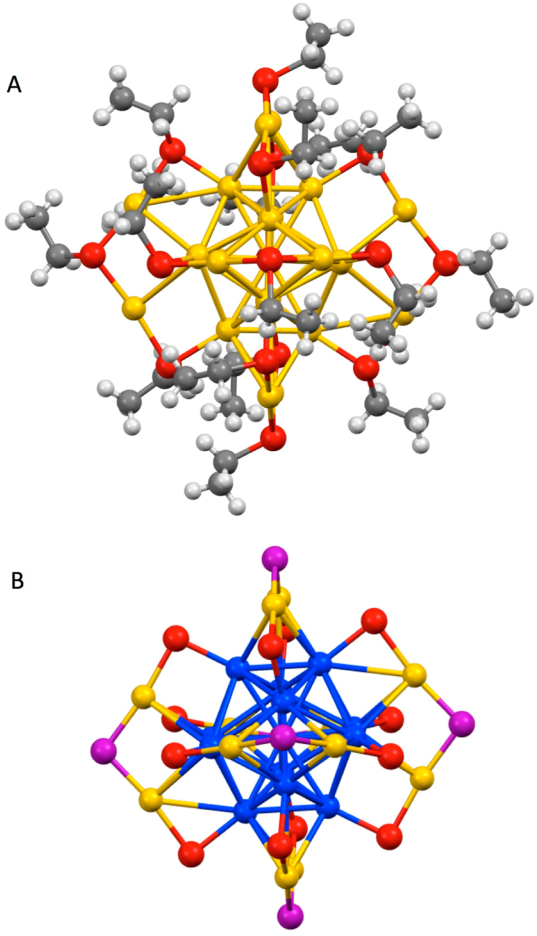

Figure 3. (A) Projection showing the X-ray crystal structure of $Au_{25}(SEt)_{18}^0$. Au = yellow, S = red, C = gray, H = white. (B) View of the twisted staple (H and C atoms removed for clarity). Au_{ico} = blue, Au_{staple} = yellow, inner-ligand S = red, outer-ligand S = purple.

$Au_{25}(SC_2H_4Ph)_{18}$, where the average distance is 3.23 and 3.22 Å for the neutral[15] and anionic cluster,[13] respectively. The outer shell of the Au_{25} cluster consists of 12 stellated Au atoms included in six half-crowns, –(SEt)–Au–(SEt)–Au–(SEt)–, where the Au atom of each –(SEt)–Au–(SEt)– structure is bound to three inner shell Au atoms and two S atoms, with the S–Au–S angle ranging from 170 to 173.5°. These Au–Au bonds, however, are longer than the icosahedral Au–Au bonds (Table 1) and could be considered to be aurophilic in nature. This feature is also present in the previously reported Au_{25} clusters,[13–15] but is missing in the Au_{13} cluster without further aurophilic bonds.[35,36] Whereas the gold cluster is not disordered (see below), the ethyl-chain carbon atoms exhibit larger thermal movement. In the solid state, weak intermolecular C–H···S hydrogen bonds (S···C distance of 3.65 Å, with C–H···S angle of 137°) join the clusters to a loose one-dimensional (1-D) chain along crystallographic (110) vector (Figure S8 in Supporting Information). A packing coefficient of 65.8% illustrates the close packing of the Au_{25} clusters.

TABLE 1. Relevant Average Bond Distances[a] in $Au_{25}(SR)_{18}$ Clusters As Obtained from Single Crystal X-ray Crystallography Structures

bond	R = Et charge = 0	R = C_2H_4Ph charge = 0 (ref 15)	R = C_2H_4Ph charge = −1 (ref 13)
$Au_{central}-Au_{ico}$[b]	2.79	2.79	2.78
$Au_{ico}-Au_{ico}$[c]	2.98	2.97	2.95
$Au_{ico}-Au_{ico}$[d]	2.79	2.78	2.80
$Au_{staple}-Au_{ico}$[e]	3.18	3.15	3.16
$S-Au_{ico}$[f]	2.37	2.38	2.37
$S-Au_{staple}$[g]	2.30	2.30	2.31

[a] All bond lengths are in angstroms; the $Au_{25}(SC_2H_4Ph)_{18}$ data were taken from the known structures,[13,15] as obtained from Cambridge Structural Database (v. 5.34 2013), The Cambridge Crystallographic Data Centre, Cambridge, U.K. (2013). [b] From the central Au atom to the 12 Au atoms of the icosahedron surface. [c] Bonds between icosahedral Au atoms not under staples. [d] Bonds between the six Au−Au pairs below the six staples. [e] Distance between stellated Au atoms and the three icosahedron Au atoms directly below. [f] S−Au bonds involving icosahedral Au atoms. [g] Bond between stellated gold and sulfur atoms.

The structure of $Au_{25}(SEt)_{18}^0$ is the first known example of single crystal X-ray crystallography structure of an Au_{25} cluster entirely protected by a short alkanethiol. It is, therefore, instructive to make a comparison with relevant parameters obtained from the structures of the corresponding phenylethanethiolate stabilized clusters. Table 1 shows some selected average bond distances.

Concerning the icosahedron, its size does not depend on ligands and charge state. Similarly, in all three structures, the bond distance between the pairs of gold atoms directly under the central sulfur atom of the six staples is also virtually constant and detectably smaller (by *ca.* 0.2 Å) than that of all other icosahedral Au−Au bonds. The distance between the stellated and the nearest icosahedron Au atoms is larger by *ca.* 0.4 Å than that between most icosahedral Au−Au bonds. No significant S−Au bond-length differences are evident among the three clusters, at least within experimental error: this observation could be relevant in gaining insights into the hypothesis of a possible Au−S bond length variation upon changing the charge state of the cluster, as detected by Raman spectroscopy.[37] A comparison between the geometry of the staples also is quite interesting. It has been observed that albeit similar, the structures of the anionic and the neutral state of $Au_{25}(SC_2H_4Ph)_{18}$ display two main differences.[15] Whereas the anionic cluster shows that all staples are distorted in the sense that the S−Au−S−Au−S motif is twisted with respect to the plane formed by the σ_h mirror in the D_{2h} subgroup of the icosahedron, none of the staples of the neutral cluster display any significant distortion. This was attributed to a possible effect of the charge state or a solid-state effect induced by the presence of the bulky counterion for the anionic state. Interestingly, however, in the neutral cluster $Au_{25}(SEt)_{18}^0$ we find two couples of linear staples (as shown in Figure 3A) and one couple (Figure 3B) displaying the same distortion mentioned above for $Au_{25}(SC_2H_4Ph)_{18}^-$; therefore, neither charge nor the presence of the counterion can be the primary cause of such a structural feature.

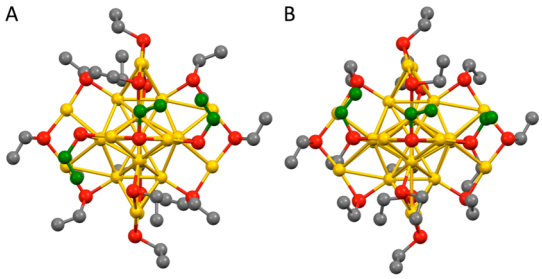

Figure 4. (A) View of the down−up−up ligand orientation in the front staple. (B) View of the up−up−up orientation. In both cases, the carbon atoms are shown in green. Hydrogen atoms removed for clarity.

From the viewpoint of the orientation of the ligands in the monolayer, another interesting feature makes all three structures different. In each staple of $Au_{25}(SC_2H_4Ph)_{18}^0$, the three ligands are oriented in a, say, down−up−down direction with respect to the plane containing the S(R)−Au−S(R)−Au−S(R) motif.[15] In $Au_{25}(SC_2H_4Ph)_{18}^-$, on the other hand, the orientation is always of the down−up−up type.[13] In $Au_{25}(SEt)_{18}^0$ we find an even different situation: whereas the ligands of two couples of staples display the same down−up−up orientation (Figure 4A) of anion $Au_{25}(SC_2H_4Ph)_{18}^-$, the third couple of staples shows the novel feature that all three ligands are oriented on the same side of the S(R)−Au−S(R)−Au−S(R) plane (Figure 4B). These comparisons clearly show that, at least in the solid state, not only charge somehow affects the structure but also the ligand type does.

ENDOR Analysis and DFT Calculations. The Davies ENDOR[33] spectrum was obtained in frozen matrix at 5.5 K for a 0.5 mM solution of $Au_{25}(SEt)_{18}^0$ in toluene. The spectrum was acquired at the field of 291.1 mT, corresponding to the maximum of the EPR signal. The spectrum shows five broad lines in the range from 0 to 90 MHz, with maxima located at 9.8, 24.7, 42.1, 60.9, and 77.9 MHz (Figure 5, red trace). The fact that the spectrum shows peaks at frequencies larger than 40 MHz is only consistent with hyperfine and quadrupolar couplings with ^{197}Au. Other possible ENDOR lines could come from the ligands' protons for which, however, the spin-density is low and lines around the proton-free Larmor frequency (12 MHz, at the magnetic field used for the ENDOR experiment) are expected. Because the number of ENDOR lines is related to the groups of equivalent Au atoms, the intriguing issue now is to explain the spectral pattern while considering that, apparently, Au_{25} clusters are composed by three such groups: central Au, 12 icosahedron Au atoms, and 12 staple Au atoms.

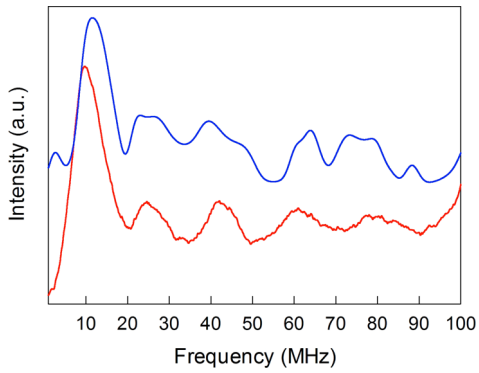

Figure 5. Davies ENDOR spectrum of a frozen 0.5 mM solution of $Au_{25}(SEt)_{18}^0$ in toluene at 5.5 K (red line). The blue line shows the corresponding simulation (vertically shifted for clarity) based on the hyperfine and quadrupole components obtained by DFT (see text). The ENDOR spectrum was recorded at a field of 291.1 mT.

To gain insights into this aspect, we carried out specific DFT calculations aimed to obtain the hyperfine and the quadrupolar tensors. We used the single crystal X-ray diffraction structure as the starting point, and the calculations were performed on two models, that is, the actual $Au_{25}(SEt)_{18}^0$ MPCs and the corresponding structure where SMe replaces SEt. The rationale was to test whether and to what extent a small ligand change could affect the quality of calculations, in comparison with an actual experimental system. This is an important aspect because, so far, accurate MPC calculations have been performed mostly on SH or SMe ligands, more or less implicitly assuming that an increase of the ligand length or change of its nature does not affect the outcome of electronic structure calculations.

The hyperfine and the quadrupole DFT-calculated tensors of $Au_{25}(SEt)_{18}^0$ were used to simulate the experimental ENDOR spectrum. The former are gathered in Table 2, while the latter and other relevant data are provided for both SEt and SMe in Tables S1 and S2 of Supporting Information. Inspection of Table 2 shows a most evident fact that the 12 Au atoms on the icosahedron surface can be divided into two groups: whereas a first group of 8 atoms (labeled as 2, 3, 4, and 5: for symmetry and with the obvious exception of the central atom, each label corresponds to two equivalent Au atoms) is characterized by strong and similar hyperfine couplings (x, y, and z averages of 41−55 MHz), a second group of 4 Au atoms (labeled as 6 and 7) have much smaller hyperfine couplings (averages of 15−17 MHz). We should also note that whereas the DFT-calculated tensors pertain to a single configuration, on the ENDOR time scale we expect the hyperfine and quadrupolar tensors of these atoms to be dynamically averaged by vibrational motion. To simulate the ENDOR response, for each group of similar core nuclei we thus used the average of each Cartesian component of the hyperfine and quadrupolar tensors, and their Euler angles. Staple nuclei have low hyperfine

TABLE 2. DFT-Computed Values of the Anisotropic Hyperfine Tensors for $Au_{25}(SEt)_{18}^0$

atom label[a]	Ax (MHz)	Ay (MHz)	Az (MHz)	ave[b] (MHz)
Au1(central)	20.7	14.2	11.6	15.5
Au4(ico)	40.3	44.5	36.7	40.5
Au3(ico)	52.8	45.1	48.5	48.8
Au7(ico)	9.1	22.7	12.6	14.8
Au2(ico)	39.5	40.8	47.6	42.6
Au5(ico)	50.8	61.6	52.7	55.0
Au6(ico)	11.4	14.3	23.9	16.5
Au8(staple)	1.9	1.9	3.1	2.3
Au11(staple)	20.0	18.6	18.9	19.2
Au9(staple)	4.0	2.9	2.8	3.2
Au10(staple)	3.7	5.0	4.3	4.3
Au12(staple)	21.0	18.3	19.4	19.6
Au13(staple)	10.3	11.1	9.8	10.4

[a] Except for the central atom, Au1, for symmetry reasons all other labels pertain to couples of equivalent Au atoms (labeling refers to the deposited structure, as also provided in the Supporting Information). [b] Average of Ax, Ay, and Az.

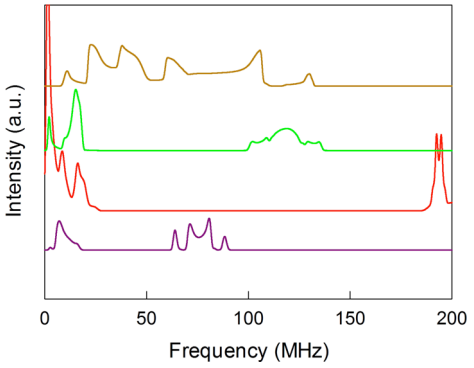

Figure 6. Simulation of the Davies ENDOR spectrum: from top to bottom, simulations pertain to the first (gold curve) and second groups of icosahedral atoms (green curve), staple Au atoms (red curve), and central atom (purple curve). The first two traces correspond to the average values. The simulations show a larger frequency range than that experimentally accessible.

couplings and, if we assume a dynamical averaging also for this group of nuclei, their main contribution is in the range 0−5 MHz of the spectrum; due to the pulse sequence used, this region is not detectable in the experimental ENDOR, and therefore, we neglected the contribution of the staple Au atoms in the simulation. The simulation for SEt (blue line in Figure 5) shows that the main features of the experimental spectrum can be reproduced quite satisfactorily. It is also worth noting that the use of average values indeed improved the quality of the simulation of the ENDOR spectrum quite significantly (Figure 5, blue line, to be compared with the results shown in Figure S5 in Supporting Information, where tensors were not averaged).

Figure 6 provides insights into the simulations for the groups of Au atoms. The results can be summarized as follows: (i) the peaks at 24.7 and 42.1 MHz are mainly

due to the first group of 8 Au core atoms, whereas (ii) the second group of 4 core atoms contributes to the strong peak at 9.8 MHz; (iii) the 77.9 MHz peak matches the simulated high-frequency structured quadrupolar peak of the central Au atom; (iv) the 60.9 MHz peak receives contributions from both the first group of core atoms and the high-frequency quadrupolar peak of the central Au atom; (v) the group of staple Au atoms only contributes to the peak at 9.8 MHz, although use of the dynamically averaged values makes its effect to the simulated peak as marginal.

In the context of ENDOR simulations, the agreement between the experimental and the predicted spectra of Figure 5 is indeed very good. In fact, it is also worth noting that the simulations carried out by using the DFT parameters obtained for the SMe ligands did not lead to the same satisfactory match with the experimental ENDOR spectrum, as illustrated in Figure S6 of Supporting Information. This is actually a quite unexpected finding because there is a general consensus about considering the effect of ligands on the MPC electronic structure as very small, at least as long as the nature of the ligand does not change significantly.[38]

The question now is as to why the 12 atoms of the icosahedral surface split into two groups. We note that the two couples of Au atoms forming the second group, and labeled as 6 and 7, correspond to those atoms for which the distance from the stellated Au atom of the same staple (see above) is the largest observed in the X-ray structure (3.31−3.35 Å). This suggests that a small disorder can cause interferences in the wave function leading to nonequivalent electron densities at the icosahedral nuclei. We also note that in the DFT-optimized structure, which is representative of the structure in a low-dielectric solvent (as the one analyzed by ENDOR), also shows disorder. In particular, the unique atoms, Au6 and Au7, form a rectangle (Figure S9 in Supporting Information) with dimensions different from those of the other two rectangles (those involving atoms Au3 with Au4 and Au2 with Au5).

CONCLUSIONS

Devising methods for obtaining relevant information about the structure of MPCs is of paramount importance for both fundamental and applied (*e.g.*, in catalysis) viewpoints. We prepared a 25-gold atom nanocluster protected by the smallest ligand ever used, ethanethiol. Its composition, charge state, and magnetic properties were assessed by a combination of MALDI-TOF, UV−vis spectroscopy, electrochemistry, and NMR spectroscopy results. The structure of $Au_{25}(SEt)_{18}^0$ could be determined precisely by X-ray crystallography analysis of high-quality single crystals. Knowledge of the exact 3D structure of $Au_{25}(SEt)_{18}^0$ allowed us to determine the relevant isotropic and anisotropic hyperfine coupling constants by DFT calculations void of those approximations associated with the use of simplified ligand models. The Davies ENDOR spectrum showed a distinct pattern that, in comparison with the DFT results, allowed us to understand that the Au atoms of the cluster can be divided into four groups: besides the central atom and the 12 staple Au atoms, the 12 icosahedron Au atoms split into a group of 8 and a group of 4 atoms. Such nonequivalence among icosahedron atoms comes from the small dissymmetries associated with dissimilar staple motifs. Such small distortions propagate into the core atoms giving rise to nonequivalent electron densities at the icosahedral nuclei and, therefore, hyperfine couplings. Pulse ENDOR thus proves to be a powerful method to study the structure and the electronic distribution of nanoclusters. The technique requires the presence of an unpaired electron and this is, in principle, always possible as long as a stable paramagnetic charge state can be attained *via* calibrated oxidation (or reduction) of an otherwise diamagnetic MPC, as others and we showed previously.[27,29−31,39]

EXPERIMENTAL SECTION

For chemicals and the synthesis of $Au_{25}(SEt)_{18}$, see Supporting Information.

UV−Vis Absorption Spectroscopy. The UV−vis spectra were obtained at 0.1 mM concentration in DCM, with 2 mm cuvettes. We used a Thermo Scientific Evolution 60S spectrophotometer or, during syntheses, an Ocean Optics QE65000 spectrophotometer equipped with a DH-2000-BAL light source. The spectra resolution was 1 or 0.8 nm, respectively.

Mass Spectrometry. MALDI-TOF mass spectra were obtained with an Applied Biosystems 4800 MALDI-TOF/TOF spectrometer equipped with a Nd:YAG laser operating at 355 nm. The laser firing rate was 200 Hz and the accelerating voltage was 25 kV. The laser pulse intensity was kept at threshold values and then progressively increased. $Au_{25}(SEt)_{18}^0$ was dissolved in benzene containing the matrix, DCTB, to obtain 0.1 mM solutions with a 1:400 MPC/matrix ratio. Two microliters of solution was drop-casted onto the sample plate and air-dried before loading into MALDI-TOF. The spectra were recorded using the reflectron positive-ion mode. As a standard, we used $Au_{25}(SC_2H_4Ph)_{18}$, which has a MW of 7394.

Electrochemistry. The experiments were carried out in DCM containing 0.1 M TBAH, under an Ar atmosphere in a glass cell thermostatted at 25 °C, unless otherwise specified. The working electrode was a glassy carbon disk (9.4×10^{-4} cm^2), prepared and activated as already described.[27] A Pt wire was the counter electrode and an Ag wire served as the quasi-reference electrode. At 25 °C, the latter has a potential of −0.187 V against the KCl saturated calomel electrode (SCE). Calibration was performed by addition of ferrocene at the end of the experiments; in the above solvent/electrolyte, the ferricenium/ferrocene redox couple has E° = 0.460 V *vs* SCE. We used a CHI 760d electrochemical workstation, and the feedback correction was applied to minimize the ohmic drop between the working and the reference electrodes.

NMR Spectroscopy. ^{1}H and ^{13}C NMR spectra were obtained at 1 mM MPC concentration in acetonitrile-d_3 or benzene-d_6 for $[n\text{-}Oct_4N^+][Au_{25}(SEt)_{18}^-]$ or $Au_{25}(SEt)_{18}^0$, respectively, with a

Bruker Avance DMX-600 MHz spectrometer equipped with a 5 mm TX-1 *x,y,z*-gradient powered, triple resonance inverse probe operating at 599.90 and 150.07 MHz, respectively. The temperature was controlled with a Bruker BVT-300 automatic temperature controller. Unless otherwise indicated, the probe temperature was maintained at 25.0 ± 0.1 °C. Chemical shifts are in parts per million (ppm) units (δ) with reference to Me_4Si used as an internal standard for both ^1H and ^{13}C NMR. To ensure a complete relaxation for all the resonances, integral values for the proton spectra were obtained by a prescan delay of 10 s. As previously done for $Au_{25}(SC_2H_4Ph)_{18}$,[30] the proton assignments were performed by standard chemical shift correlations as well as by 2D correlation spectroscopy (COSY), total correlation spectroscopy (TOCSY), and nuclear Overhauser enhancement spectroscopy (NOESY) experiments; the ^{13}C chemical shift values were obtained and assigned through 2D-heteronuclear correlation experiments (heteronuclear multiple quantum coherence, HMQC).

X-ray Single Crystal Diffraction. Crystallographic data of $Au_{25}(SEt)_{18}$ were collected at 123 K with Cu Kα radiation (λ = 1.54184 Å) on an Agilent SuperNova dual wavelength diffractometer equipped with Atlas CCD area detector. CrysAlisPro[40] software was employed for the data measurements and processing. The structure was solved by direct methods integrated in the program of Olex^2,[41] and full-matrix least-squares refinements on F^2 were performed using SHELXL.[42] Analytical numeric absorption correction[43] was applied to treat the reflections. Due to slight disorder, distances restraints were applied for all the ethyl groups. For H atoms, except for those attached to C2, C6, and C8, all the others were calculated to their idealized positions with constraint isotropic thermal factors [1.2 or 1.5 times of U_{eq}(C)] and refined as riding atoms. The H atoms bonded to C2, C6, and C8 were fixed at calculated positions, as the riding mode refinement could not reach convergence. For crystal data and refinement results see Supporting Information. The crystal structure has been deposited to the Cambridge Crystallographic Data Centre with CCDC number of 984217 and the data can be obtained free of charge *via* www.ccdc.cam.ac.uk/data_request/cif.

ENDOR Spectroscopy. The ^{197}Au ENDOR spectrum was recorded with a Bruker Elexsys E580 spectrometer equipped with a pulse ENDOR dielectric probe head and an Oxford CF935 cryostat. The 0.5 mM solutions of $Au_{25}(SEt)_{18}^0$ in toluene were introduced into 3 (o.d.) × 2 mm (i.d.) quartz tubes, degassed by several freeze-pump thaw cycles, and sealed off under vacuum (5×10^{-5} Torr). The samples were then rapidly cooled down to 80 K, and the actual measurements were finally carried out at 5.5 K. We used the Davies ENDOR pulse sequence, with 32 ns of microwave inversion pulse and 16−32 ns pulse sequence for echo detection. The radiofrequency pulse was 4 μs long and was amplified by a 500 W Bruker RF amplifier. The frequency range was limited to below 100 MHz to avoid frequency artifacts. With the use of the DFT values as input for the nucleus-electron interaction Hamiltonian, ENDOR simulations were performed with the EasySpin software program[44] working on the MatLab 7.12 calculation environment.

Computational Methods. Starting from the X-ray structure, the $Au_{25}(SEt)_{18}$ cluster was optimized using DFT as implemented in Turbomole V6.3.1.[45] For the energy minimization step, we employed the s-vwn functional and def2-TZVP basis set for all atoms with a def2-ecp effective core potential for all Au atoms. At the optimized geometry, hyperfine constants and quadrupole tensors were calculated using Orca 2.9.1.[46] These calculations were carried out using unrestricted DFT with the GGA functional (BP86), the TZVP basis set for Au, and the DZP basis set for all other atoms. Scalar relativistic effects were introduced using Zeroth-Order Regular Approximation (ZORA).[47] All core electrons were included explicitly in the calculation of hyperfine and quadrupolar tensors, using the segmented all-electron relativistically constructed (SARC) basis set.[48] The Orca-euler utility program was used to calculate the Euler rotation of the hyperfine tensor and the electric field gradient tensor with respect to the g-tensor.

Conflict of Interest: The authors declare no competing financial interest.

Acknowledgment. This work was financially supported by AIRC (F.M., Project 12214: Innovative Tools for Cancer Risk Assessment and Early Diagnosis −5 per mille), the Academy of Finland (K.R., Grants No. 263256 and 265328), and the National Science Foundation (J.A.G., CAREER Award CHE-0847340).

Supporting Information Available: Further details on the synthesis and characterization of $Au_{25}(SEt)_{18}$, ENDOR analysis, DFT-derived structures, and X-ray crystallography information, including structure and corresponding checkCIF file. This material is available free of charge via the Internet at http://pubs.acs.org.

REFERENCES AND NOTES

1. Murray, R. W. Nanoelectrochemistry: Metal Nanoparticles, Nanoelectrodes, and Nanopores. *Chem. Rev.* **2008**, *108*, 2688–2720.
2. Tsukuda, T. Toward an Atomic-Level Understanding of Size-Specific Properties of Protected and Stabilized Gold Clusters. *Bull. Chem. Soc. Jpn.* **2012**, *85*, 151–168.
3. Qian, H.; Zhu, M.; Wu, Z.; Jin, R. Quantum Sized Gold Nanoclusters with Atomic Precision. *Acc. Chem. Res.* **2012**, *45*, 1470–1479.
4. Negishi, Y.; Kurashige, W.; Niihori, Y.; Nobusada, K. Toward the Creation of Stable, Functionalized Metal Clusters. *Phys. Chem. Chem. Phys.* **2013**, *15*, 18736–18751.
5. Cossaro, A.; Mazzarello, R.; Rousseau, R.; Casalis, L.; Verdini, A.; Kohlmeyer, A.; Floreano, L.; Scandolo, S.; Morgante, A.; Klein, M. L.; *et al.* X-ray Diffraction and Computation Yield the Structure of Alkanethiols on Gold(111). *Science* **2008**, *321*, 943–946.
6. Jiang, D. The Expanding Universe of Thiolated Gold Nanoclusters and Beyond. *Nanoscale* **2013**, *5*, 7149–7160.
7. Häkkinen, H. The Gold−Sulfur Interface at the Nanoscale. *Nat. Chem.* **2012**, *4*, 443–455.
8. Pensa, E.; Cortéz, E.; Corthey, G.; Carro, P.; Vericat, C.; Fonticelli, M. H.; Benitez, G.; Rubert, A. A.; Salvarezza, R. C. The Chemistry of the Sufur−Gold Interface: In Search of a Unified Model. *Acc. Chem. Res.* **2012**, *45*, 1183–1192.
9. Jadzinsky, P. D.; Calero, G.; Ackerson, C. J.; Bushnell, D. A.; Kornberg, R. D. Structure of a Thiol Monolayer-Protected Gold Nanoparticle at 1.1 Å Resolution. *Science* **2007**, *318*, 430–433.
10. Qian, H.; Eckenhoff, W. T.; Zhu, Y.; Pintauer, T.; Jin, R. Total Structure Determination of Thiolate-Protected Au_{38} Nanoparticles. *J. Am. Chem. Soc.* **2010**, *132*, 8280–8281.
11. Zeng, C.; Qian, H.; Li, T.; Li, G.; Rosi, N. L.; Yoon, B.; Barnett, R. N.; Whetten, R. L.; Landman, U.; Jin, R. Total Structure and Electronic Properties of the Gold Nanocrystal $Au_{36}(SR)_{24}$. *Angew. Chem., Int. Ed.* **2012**, *51*, 13114–13118.
12. Zeng, C.; Li, T.; Das, A.; Rosi, N. L.; Jin, R. Chiral Structure of Thiolate-Protected 28-Gold-Atom Nanocluster Determined by X-ray Crystallography. *J. Am. Chem. Soc.* **2013**, *135*, 10011–10013.
13. Heaven, M. W.; Dass, A.; White, P. S.; Holt, K. M.; Murray, R. W. Crystal Structure of the Gold Nanoparticle $[N(C_8H_{17})_4][Au_{25}(SCH_2CH_2Ph)_{18}]$. *J. Am. Chem. Soc.* **2008**, *130*, 3754–3755.
14. Zhu, M.; Aikens, C. M.; Hollander, F. J.; Schatz, G. C.; Jin, R. Correlating the Crystal Structure of a Thiol-Protected Au_{25} Cluster and Optical Properties. *J. Am. Chem. Soc.* **2008**, *130*, 5883–5885.
15. Zhu, M.; Eckenhoff, W. T.; Pintauer, T.; Jin, R. Conversion of Anionic $[Au_{25}(SCH_2CH_2Ph)_{18}]^-$ Cluster to Charge Neutral Cluster *via* Air Oxidation. *J. Phys. Chem. C* **2008**, *112*, 14221–14224.
16. Das, A.; Li, T.; Nobusada, K.; Zeng, C.; Rosi, N. L.; Jin, R. Nonsuperatomic $[Au_{23}(SC_6H_{11})_{16}]^-$ Nanocluster Featuring Bipyramidal Au_{15} Kernel and Trimeric $Au_3(SR)_4$ Motif. *J. Am. Chem. Soc.* **2013**, *135*, 18264–18267.
17. Dass, A.; Stevenson, A.; Dubay, G. R.; Tracy, J. B.; Murray, R. W. Nanoparticle MALDI-TOF Mass Spectrometry without Fragmentation: $Au_{25}(SCH_2CH_2Ph)_{18}$ and Mixed Monolayer $Au_{25}(SCH_2CH_2Ph)_{18-x}(L)_x$. *J. Am. Chem. Soc.* **2008**, *130*, 5940–5946.

18. Negishi, Y.; Nobusada, K.; Tsukuda, T. Glutathione-Protected Gold Clusters Revisited: Bridging the Gap between Gold(I)−Thiolate Complexes and Thiolate-Protected Gold Nanocrystals. *J. Am. Chem. Soc.* **2005**, *127*, 5261–5270.
19. Tracy, J. B.; Kalyuzhny, G.; Crowe, M. C.; Balasubramanian, R.; Choi, J.-P.; Murray, R. W. Poly(ethylene glycol) Ligands for High-Resolution Nanoparticle Mass Spectrometry. *J. Am. Chem. Soc.* **2007**, *129*, 6706–6707.
20. Parker, J. F.; Fields-Zinna, C. A.; Murray, R. W. The Story of a Monodisperse Gold Nanoparticle: $Au_{25}L_{18}$. *Acc. Chem. Res.* **2010**, *43*, 1289–1296.
21. Tlahuice-Flores, A.; Santiago, U.; Bahena, D.; Vinogradova, E.; Conroy, C. V.; Ahuja, T.; Bach, S. B. H.; Ponce, A.; Wang, G.; José-Yacamán, M.; *et al.* Structure of the Thiolated Au_{130} Cluster. *J. Phys. Chem. A* **2013**, *117*, 10470–10476.
22. Tang, Z.; Robinson, D. A.; Bokossa, N.; Xu, B.; Wang, S.; Wang, G. Mixed Dithiolate Durene-DT and Monothiolate Phenylethanethiolate Protected Au_{130} Nanoparticles with Discrete Core and Core-Ligand Energy States. *J. Am. Chem. Soc.* **2011**, *133*, 16037–16044.
23. Negishi, Y.; Sakamoto, C.; Tatsuya, O.; Tsukuda, T. Synthesis and the Origin of the Stability of Thiolate−Protected Au_{130} and Au_{187} Clusters. *J. Phys. Chem. Lett.* **2012**, *3*, 1624–1628.
24. Bahena, D.; Bhattarai, N.; Santiago, U.; Tlahuice, A.; Ponce, A.; Bach, S. B. H.; Yoon, B.; Whetten, R. L.; Landman, U.; José-Yacamán, M. STEM Electron Diffraction and High-Resolution Images Used in the Determination of the Crystal Structure of the $Au_{144}(SR)_{60}$ Cluster. *J. Phys. Chem. Lett.* **2013**, *4*, 975–981.
25. Koivisto, J.; Salorinne, K.; Mustalahti, S.; Lahtinen, T.; Malola, S.; Häkkinen, H.; Pettersson, M. Vibrational Perturbations and Ligand−Layer Coupling in a Single Crystal of $Au_{144}(SC_2H_4Ph)_{60}$ Nanocluster. *J. Phys. Chem. Lett.* **2014**, *5*, 387–392.
26. Lee, D.; Donkers, R. L.; Wang, G.; Harper, A. S.; Murray, R. W. Electrochemistry and Optical Absorbance and Luminescence of Molecule-like Au_{38} Nanoparticles. *J. Am. Chem. Soc.* **2004**, *126*, 6193–6199.
27. Antonello, S.; Perera, N. V.; Ruzzi, M.; Gascón, J. A.; Maran, F. Interplay of Charge State, Lability, and Magnetism in the Molecule-like $Au_{25}(SR)_{18}$ Cluster. *J. Am. Chem. Soc.* **2013**, *135*, 15585–15594.
28. Antonello, S.; Holm, A. H.; Instuli, E.; Maran, F. Molecular Electron-Transfer Properties of Au_{38} Clusters. *J. Am. Chem. Soc.* **2007**, *129*, 9836–9837.
29. Zhu, M.; Aikens, C. M.; Hendrich, M. P.; Gupta, R.; Qian, H.; Schatz, G. C.; Jin, R. Reversible Switching of Magnetism in Thiolate-Protected Au_{25} Superatoms. *J. Am. Chem. Soc.* **2009**, *131*, 2490–2492.
30. Venzo, A.; Antonello, S.; Gascón, J. A.; Guryanov, I.; Leapman, R. D.; Perera, N. V.; Sousa, A.; Zamuner, M.; Zanella, A.; Maran, F. Effect of the Charge State ($z = -1, 0, +1$) on the Nuclear Magnetic Resonance of Monodisperse $Au_{25}[S(CH_2)_2Ph]_{18}^{z}$ Clusters. *Anal. Chem.* **2011**, *83*, 6355–6362.
31. Antonello, S.; Arrigoni, G.; Dainese, T.; De Nardi, M.; Parisio, G.; Perotti, L.; René, A.; Venzo, A.; Maran, F. Electron Transfer through 3D Monolayers on Au_{25} Clusters. *ACS Nano* **2014** DOI: 10.1021/nn406504k. http://dx.doi.org/10.1021/nn406504k.
32. Weil, J. A.; Bolton, R. J. Double-Resonance Techniques. *Electron Paramagnetic Resonance: Elementary Theory and Practical Applications*, 2nd ed.; Wiley-Interscience: Hoboken, NJ, 2007; pp 385−413.
33. Davies, E. R. A New Pulse ENDOR Technique. *Phys. Lett.* **1974**, *47A*, 1–2.
34. Van Willigen, H.; Van Rens, J. G. M. Quadrupole Effects on the Hyperfine Structure of a Gold(II) Complex. *Chem. Phys. Lett.* **1968**, *2*, 283–285.
35. Briant, C. E.; Theobald, B. R. C.; White, J. W.; Bell, L. K.; Mingos, D. M. P.; Welch, A. J. Synthesis and X-ray Structural Characterization of the Centred Icosahedral Gold Cluster Compound $[Au_{13}(PMe_2Ph)_{10}Cl_2](PF_6)_3$; the Realization of a Theoretical Prediction. *Chem. Soc., Chem. Commun.* **1981**, 201–202.
36. Shichibu, Y.; Konishi, K. HCl-Induced Nuclearity Convergence in Diphosphine-Protected Ultrasmall Gold Clusters: A Novel Synthetic Route to "Magic-Number" Au_{13} Clusters. *Small* **2010**, *10*, 1216–1220.
37. Parker, J. F.; Choi, J.-P.; Wang, W.; Murray, R. W. Electron Self-Exchange Dynamics of the Nanoparticle Couple $[Au_{25}(SC_2Ph)18]^{0/1-}$ by Nuclear Magnetic Resonance Line-Broadening. *J. Phys. Chem. C* **2008**, *112*, 13976–13981.
38. Tlahuice-Flores, A.; Whetten, R. L.; Jose-Yacaman, M. Ligand Effects on the Structure and the Electronic Optical Properties of Anionic $Au_{25}(SR)_{18}$ Clusters. *J Phys. Chem. C* **2013**, *117*, 20867–20875.
39. McCoy, R. S.; Choi, S.; Collins, G.; Ackerson, B. J.; Ackerson, C. J. Superatom Paramagnetism Enables Gold Nanocluster Heating in Applied Radiofrequency Fields. *ACS Nano* **2013**, *7*, 2610–2616.
40. *CrysAlisPro*, version 1.171.36.28; Agilent Technologies Ltd: Yarnton, England, 2013.
41. Dolomanov, O. V.; Bourhis, L. J.; Gildea, R. J.; Howard, J. A. K.; Puschmann, H. OLEX2: A Complete Structure Solution, Refinement and Analysis Program. *J. Appl. Crystallogr.* **2009**, *42*, 339–341.
42. Sheldrick, G. M. A Short History of SHELX. *Acta Crystallogr.* **2008**, *A64*, 112–122.
43. Clark, R. C.; Reid, J. S. The Analytical Calculation of Absorption in Multifaceted Crystals. *Acta Crystallogr.* **1995**, *A51*, 887–897.
44. Stoll, S.; Schweiger, A. EasySpin, a Comprehensive Software Package for Spectral Simulation and Analysis in EPR. *J. Magn. Reson.* **2006**, *178*, 42–55.
45. Ahlrichs, R.; Bär, M.; Häser, M.; Horn, H.; Kölmel, C. Electronic Structure Calculations on Workstation Computers: The Program System Turbomole. *Chem. Phys. Lett.* **1989**, *162*, 165–169.
46. Neese, F. The ORCA Program System. *Wiley Interdiscip. Rev.: Comput. Mol. Sci.* **2012**, *2*, 73–78.
47. van Wüllen, C. Molecular Density Functional Calculations in the Regular Relativistic Approximation: Method, Application to Coinage Metal Diatomics, Hydrides, Fluorides and Chlorides, and Comparison with First-Order Relativistic Calculations. *J. Chem. Phys.* **1998**, *109*, 392–399.
48. Pantazis, D. A.; Chen, X.-Y.; Landis, C. R.; Neese, F. All-Electron Scalar Relativistic Basis Sets for Third-Row Transition Metal Atoms. *J. Chem. Theory Comput.* **2008**, *4*, 908–919.